





Charge-based Capacitive Self-Sensing with Continuous State Observation for Resonant Electrostatic MEMS Mirrors

Richard Schroedter , Han Woong Yoo , Member, IEEE David Brunner , and Georg Schitter  Senior Member, IEEE

Abstract—This contribution presents charge-based capacitive self-sensing with a continuous full state observer for a parametrically driven resonant electrostatic 1D MEMS mirror considering precise and seamless estimation. Based on current integrators, series capacitances or a capacitance network the direct charge self-sensing principles are investigated and compared considering leakage currents, precision and a minimum implementation effort. In comparison to the other charge sensing methods, the proposed methods directly measure the charge changes while the drive voltage is switched on. Since resonant MEMS mirrors are driven by a rectangular signal, the direct self-sensing implies a lack of data when the drive voltage is switched off. A nonlinear observer is also proposed to estimate the full mirror state continuously based on an identified MEMS mirror model. The capacitive charge self-sensing methods achieve overall a high sensing precision of less than 0.14 % RMSE and the observer estimation error of the full state is below 1 % peak-to-peak error regardless of the availability of the charge self-sensing measurements, demonstrates accurate continuous full state estimation.

Index Terms—charge-based capacitive self-sensing, resonant MEMS mirror, electrostatic comb drive, switched current integrator, capacitance network, nonlinear switched input Luenberger observer

I. INTRODUCTION

MEMS mirrors are increasingly applied in various mobile precision scanning application due to their light weight, low power consumption, high repeatability and standard CMOS mass production capability [1], [2]. Applications include automotive and industrial lidar [3], [4], head-mounted displays (HMDs) [5], head-up displays (HUDs) [6] or projectors [7] and external cavity quantum cascade lasers (EC-QCLs) [8] as well as endoscopy [9]. For ensuring high precision scanning and robustness the MEMS scanning system requires feedback sensors for synchronization of multiple axis [7] or multiple scanners [10], [11], e.g. performing a 2D Lissajous or raster scan, as well as stabilizing resilience towards shock and vibration [12], [13]. Optical sensing methods are widely used for calibration purposes [14]–[16], but suffer from bulky and complex packaging for system integration [17]. Piezoresistive

[18] and piezoelectric [19] sensors can be designed for high sensitive feedback, but are both temperature dependent, require additional material processing steps and can show signs of fatigue for a long term operation. In addition, the most common piezoelectric materials are CMOS incompatible [20].

In contrast, capacitive sensing methods like charge and current sensing directly measure the electrostatic drive comb capacitance or additional comb structures itself. If single crystalline silicon material is used, low internal stress results in extreme high repeatability, while the self-sensing method is expected to be comparably insensitive towards temperature changes. Consequently, capacitive self-sensing can provide an efficient angle feedback for MEMS mirrors considering harsh environmental influences like in automotive lidar applications [3]. Charge-sensing, commonly referred to as capacitive sensing or capacitance to voltage converter (C2V), is a common technique in MEMS accelerators and gyroscopes, [21], [22]. These implementations profit from asymmetric variable capacitances in a bridge circuit, which is typically not available for MEMS mirrors. Furthermore, continuous-time voltage-mode capacitive sensing is presented in [23] with a subsequent modulation of the drive voltage. Another switched capacitor charge amplification is presented in [24] using a fast switching mode, but not continuous in time. General descriptions to the circuits presented in this paper are given as the switched capacitor sensing method in [25], for ultrasonic transducer in [26] and the voltage buffer circuit with voltage follower in [27].

For categorizing capacitive sensing readouts, the methods are classified as follows: Firstly, charge-based sensing measures the charge on the capacitance, mostly with a current integrator (CI) or charge-to-voltage converter, while current-based sensing methods measure the current, mostly with a transimpedance amplifier (TIA). Secondly, direct sensing methods measure accumulate charge or current for a certain period using a reference or actuation voltage, while modulation based methods add a modulation voltage on top on the reference or actuation voltage. Thirdly, the self-sensing term is applied for topologies, where driving and sensing is performed on the same structure, i.e. the electrostatic comb drive.

Current sensing with additional sensing combs is presented for resonant MEMS mirrors in [28], [29]. High resistive current self-sensing is presented in [30] although with low phase resolution. Highly stiffening resonant MEMS mirrors operated in a bifurcated upper response curve allow current self-sensing

Manuscript received June 14, 2021; revised July 28, 2021; accepted August 17, 2021. This work has been supported in part by the Austrian Research Promotion Agency (FFG) under the scope of the AUTOScan project (FFG project number 884345). (Corresponding author: Richard Schroedter, e-mail: schroedter@acin.tuwien.ac.at) All authors are with the Automation and Control Institute (ACIN), TU Wien, Gusshausstrasse 27-29, 1040 Vienna, Austria.

using the zero angle crossing, which provides highly precise phase information [31], [32]. However, direct current self-sensing is limited to high frequency MEMS mirrors, while low frequency or quasi-static MEMS mirrors feature too small displacement currents [32], [33]. Modulation-based self-sensing applies a high frequency (at two orders of magnitude above the resonance, which is typically in the MHz range) carrier voltage onto the drive voltage of the MEMS mirror [7], [34], [35]. This provides a continuous angle signal, but the modulation and demodulation increase power consumption and require complex strategies to reduce feed-through coupling from the drive voltage [36], [37]. So far, the only direct charge-based capacitive self-sensing for MEMS mirrors was presented in [38], but this method detects only a single point of the capacitance per period and thus does not exploit the full information of the charge change. Using the full charge curve direct capacitive self-sensing is firstly proposed by the authors in [39]. The charge curve is measured and evaluated during high voltage on time and fed to an observer to estimate the mirror state at all time.

This paper presents a precise angle estimation method for resonant electrostatic MEMS mirrors based on charge self-sensing and demonstrates three variants of a prototype implementation. The experimentally proven sensing methods can be applied independently of the phase relation as well of the eigenfrequency of the mirror. As extension to [39] a precise leakage model for the current integrator circuit is developed, which leads to an accuracy improvement by a factor of two. Based on a switched observer design, the full state results are provided, which can be used for the sensing principle available for continuous time feedback control, e.g. for synchronization and increasing robustness.

This paper is organized as follows. In Section II the charge self-sensing principles are introduced. Section III describes the MEMS mirror model and the observer with switched input. In Section IV the experimental verification of the charge sensing methods for a 1D resonant MEMS mirror are presented including parameter identification and simulation of the observer with switched input. In Section V the performance of the sensing methods and the achieved result are discussed. Section VI concludes the contribution of the paper.

II. DIRECT CHARGE SELF-SENSING

Voltage driven electrostatic MEMS mirrors can be self-sensed by the transducers charge or displacement current [40]. The charge and current on variable capacitance $C(\theta)$ are denoted by

$$q = \int i dt = C(\theta) v, \quad i = \frac{dq}{dt} = \frac{dC(\theta)}{d\theta} \dot{\theta} v + C(\theta) \dot{v} \quad (1)$$

with θ being the mirror deflection angle. For a given drive voltage v the mirror movement is defined by its charge or current respective capacitance change. Assume an electrostatically actuated MEMS mirror with a voltage driven movable mirror and two stator electrodes having an offset as is depicted in Fig. 1a and its equivalent circuit in Fig. 1b respectively. The overlap area $A(\theta)$ of the comb drives (cf. dark gray area in Fig. 1a) defines two capacitances with approximately

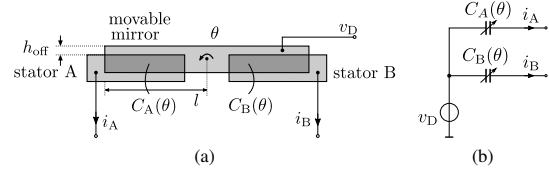


Fig. 1. MEMS mirror with electrostatic comb drive: (a) comb electrode configuration, (b) equivalent circuit

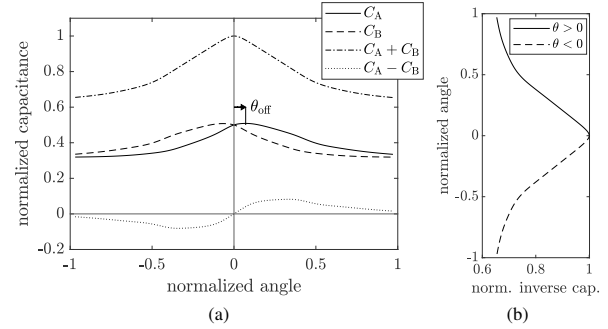


Fig. 2. (a) Normalized capacitances over angle demonstrating the capacitance peak shift θ_{off} by the offset h_{off} , (b) inverse sum capacitance $(C_A + C_B)^{-1}$

$C(\theta) \approx \epsilon A(\theta)/g$, where g is the gap between the comb drive fingers. Fig. 2 illustrates the two capacitances $C_A(\theta)$ and $C_B(\theta)$, which decreases for higher angle while fringe fields flatten the steepness. If the stator electrode has a small offset h_{off} toward the mirror electrode, e.g. a multi-layer device [39], [41], [42], then the direction can be detected by the difference of the currents or charges respectively. This is illustrated in Fig. 2 with the difference capacitance $C_A(\theta) - C_B(\theta)$ resulting from the offset angle $\theta_{\text{off}} \approx h_{\text{off}}/l$, where l is the finger length to the rotation axis.

For measuring the charge changes on the comb electrode driven by a voltage three concept variants as shown in Fig. 3 are proposed. The comb drive capacitances store the charges according to the instantaneous deflection angle and applied voltage. Resonant tilting MEMS mirrors are manufactured with initial in-plane configuration and typically driven with rectangular voltage switching between $v_D = v_{\text{drive}}$ and $v_D = 0$, where the voltage-off time permits the free out-of-plane oscillation. For $v_D = 0$ all charge immediately flows away through the driver and no charge $q = C(\theta) v_D = 0$ is kept on the comb drive to be detected. Consequently, during this time no charge sensing signal is available. However, the voltage off time can be used to reset the charging capacitances C_{int} or C_1 , C_2 and C_{1n} , C_{2n} , C_{3n} respectively, to avoid long term loading effects.

a) *Current integrator*: The charges can be measured using an operational amplifier with capacitance feedback as depicted in Fig. 3a. The inverting integrator circuit creates the charge equivalent voltages

$$v_A = -\frac{1}{C_{\text{int}}} \int i_A dt, \quad v_B = -\frac{1}{C_{\text{int}}} \int i_B dt \quad (2)$$

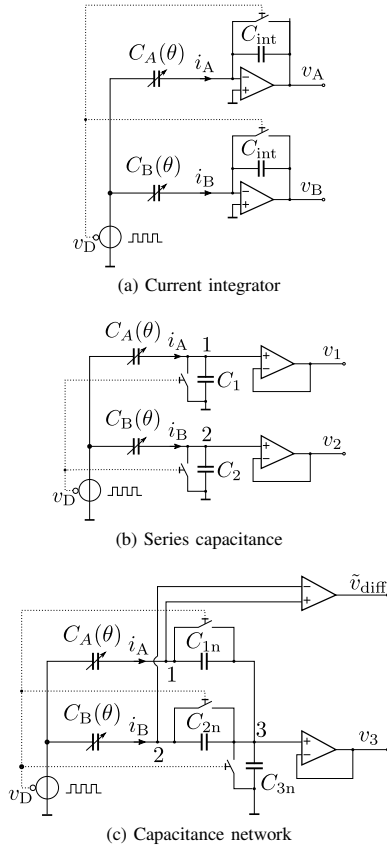


Fig. 3. Charge sensing principles, where $C_A(\theta)$ and $C_B(\theta)$ are the deflection dependent comb drive capacitances: (a) current integrator, (b) series capacitances, (c) capacitance network. A TTL signal is provided in phase to the drive voltage for the reset switches during HV off time.

and with (1)

$$v_A(\theta) = -\frac{C_A(\theta)}{C_{\text{int}}} v_D, \quad v_B(\theta) = -\frac{C_B(\theta)}{C_{\text{int}}} v_D. \quad (3)$$

Typically, C_{int} and v_D are given by design, while the variable MEMS capacitances are calibrated. To obtain the deflection angle, the voltage functions (3) need to be inverted. While each individual capacitance curve has an asymmetry from the offset, the sum capacitance of both electrodes

$$C(\theta) = C_A(\theta) + C_B(\theta) \quad (4)$$

is symmetric and invertible due to the unique correspondence of angle and voltage for at least one side of the trajectory as shown in Fig. 2. Negative or positive angle direction is then given by the difference voltage provides by the difference capacitance $C_A(\theta) - C_B(\theta)$. Therefore, the voltages (3) are summed to

$$v_{\text{sum}} = v_A + v_B, \quad v_{\text{diff}} = v_A - v_B. \quad (5)$$

Consequently, the deflection angle can be identified by

$$\theta = \text{sign}(v_{\text{diff}}) \cdot C^{-1} \left(\frac{C_{\text{int}} |v_{\text{sum}}|}{v_D} \right), \quad \text{for } v_D \neq 0, \quad (6)$$

where C^{-1} maps capacitance to angle, cf. as shown in Fig. 2b.

b) Series capacitance: Fig. 3b demonstrates an similar but passive charge sensing circuit with series capacitances, that requires no operational amplifier for integration. At the nodes 1 and 2 the voltages are given by

$$v_1(\theta) = v_D \frac{C_A(\theta)}{C_A(\theta) + C_1}, \quad v_2(\theta) = v_D \frac{C_B(\theta)}{C_B(\theta) + C_2}. \quad (7)$$

However, the series capacitances lead to a voltage drop at the MEMS capacitance due to the voltage divider (cf. Fig. 4b (top)). A trade-off is chosen here to minimize the reduced driving voltage but increase the sensing signal for high SNR. The integrating capacitances C_1 and C_2 are chosen by orders of magnitude higher than the comb capacitances. The deflection angle is calculated analog to (6) with $v_{\text{sum}} = v_1 + v_2$ and $v_{\text{diff}} = v_1 - v_2$.

c) Capacitance network: The capacitance network shown in Fig. 3c is built similar to the series capacitances with C_{1n} and C_{2n} , but with an additional capacitance C_{3n} , which creates the summation node 3. The difference voltage of the nodes 1 and 2 is related to the direction of the oscillation with

$$\tilde{v}_{\text{diff}} = \frac{v_1}{1 - \frac{v_1}{v_D}} - \frac{v_2}{1 - \frac{v_2}{v_D}} \approx v_1 - v_2. \quad (8)$$

At node 3 the voltage provides directly the sum signal of both comb electrodes with

$$v_3 = \frac{v_D}{1 + \frac{C_{3n}}{C_{\text{net}}(\theta)}}, \quad C_{\text{net}}(\theta) = \frac{1}{\frac{1}{C_A(\theta)} + \frac{1}{C_{1n}}} + \frac{1}{\frac{1}{C_B(\theta)} + \frac{1}{C_{2n}}}. \quad (9)$$

Consequently, the deflection angle can be calculated by

$$\theta = \text{sign}(\tilde{v}_{\text{diff}}) \cdot C_{\text{net}}^{-1} \left(\frac{C_{3n} v_3}{v_D - v_3} \right), \quad \text{for } v_D \neq 0. \quad (10)$$

To realize this circuit, C_1 and C_2 are chosen much larger than C_3 enabling high SNR for the sum signal, while C_3 is much larger than the MEMS capacitances to cause a small voltage drop only. In comparison to the series capacitance circuit, the network requires only a single high precision sensing channel with ADC, while the direction is given by the difference as a binary switch.

Fig. 4 illustrates the ideal signals of the three charge sensing methods based on a simulation in Matlab/Simscape. The active charge integrator circuit provides negative sensing signals without any voltage drop ($v_D - v_1$ and $v_D - v_2$) on the comb actuator, cf. Fig. 4a with $C_{\text{int}} = 100$ pF. The passive series capacitances show an inevitable voltage drop of the driving signal, cf. Fig. 4b with $C_1 = C_2 = 100$ pF. The passive capacitance network provides directly the sum (v_3) and difference signal enabling simple digital direction detection by its sign, cf. Fig. 4c with $C_{1n} = C_{2n} = 1000$ pF, $C_{3n} = 100$ pF, where \tilde{v}_{diff} is the difference $v_{1n} - v_{2n}$ amplified by factor 20. According to the voltage off switching no sensing signal is available and the integrating capacitances are reset, cf. Fig. 3.

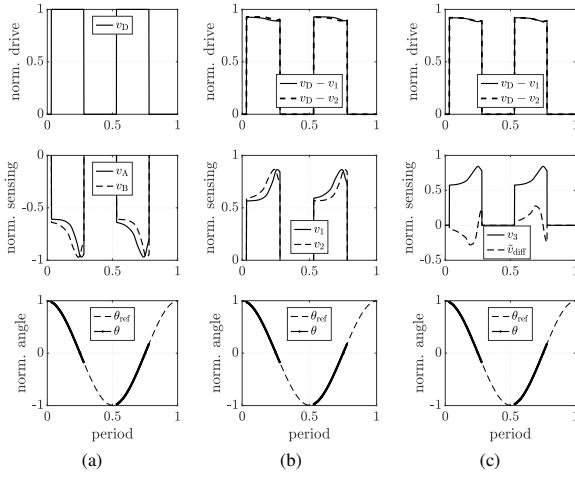


Fig. 4. Ideal drive, sensing and angle signals: (a) current integrator, (b) series capacitances, (c) capacitance network

III. MODELING AND OBSERVER

To provide an angle at all time for feedback control, a switched observer updated during voltage on-time estimates the mirror state [39].

A. MEMS mirror model

The resonant MEMS mirror is modeled with a single degree of freedom nonlinear oscillation differential equation [43]

$$\ddot{\theta} + \underbrace{\frac{c_n(\theta, \dot{\theta})}{J}}_{\tilde{c}_n(\theta, \dot{\theta})} \dot{\theta} + \underbrace{\frac{k_n(\theta)}{J}}_{\tilde{k}_n(\theta)} \theta = \underbrace{\frac{1}{2J} \frac{\partial C(\theta)}{\partial \theta}}_{\tilde{C}'(\theta)} v^2, \quad (11)$$

where J denotes the torque inertia including the mirror and all moving drive combs, $c_n(\theta, \dot{\theta})$ is a nonlinear damping and $k_n(\theta)$ a high order nonlinear stiffness. The nonlinear stiffness

$$k_n(\theta) = k_0 + k_2 \theta^2 + k_4 \theta^4 + k_6 \theta^6, \quad (12)$$

is caused by the leaf-spring design, cf. [44], and leads to a nonlinear frequency amplitude behavior with bifurcations [43]. Furthermore, squeeze-film and finger damping (cf. [45], [46]) is modeled as nonlinear amplitude depended damping with

$$c_n(\Theta) = c_0 + c_1 \Theta + c_2 \Theta^2 + \dots + c_6 \Theta^6, \quad (13)$$

where Θ denotes the current amplitude of the oscillation [43]. For implementation of an amplitude dependent damping from given oscillation data, an amplitude equivalent h is introduced, which estimates the deflection angle amplitude by the low-pass filtered squared velocity as proposed in [43]:

$$\ddot{h}(t) + 2\omega_h \dot{h}(t) + \omega_h^2 h(t) = \omega_h^2 \dot{\theta}^2(t) \quad (14)$$

Consequently, (13) is redefined as amplitude dependent damping function in terms of h using (14) as follows:

$$\tilde{c}_h(h) = \tilde{c}_0 + \tilde{c}_1 h + \tilde{c}_2 h^2 + \dots + \tilde{c}_6 h^6, \quad (15)$$

As verified in [43], this model provides an adequate representation of the MEMS mirror behavior.

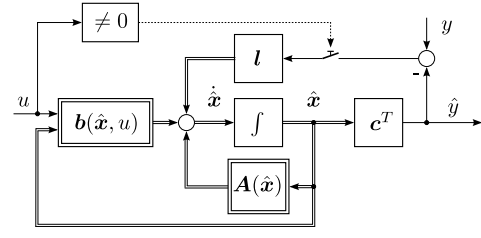


Fig. 5. Nonlinear extended Luenberger observer with switched input (16), (18), whose correction by gain l is enabled for a non-zero drive input [39], where u equals to the drive voltage v_D and y represent the angle θ estimated from the charge sensing signal (6)

B. Nonlinear observer with switched input

The nonlinear extended Luenberger observer for the MEMS mirror is sketched in Fig. 5, where the observer error $\hat{e} = y - \hat{y}$ is switched to zero if the voltage input u is zero. According to the nonlinear oscillator differential equation (11) the nonlinear observer is designed in state-space representation [39] as follows:

$$\dot{\hat{x}} = A(\hat{x}) \cdot \hat{x} + b(\hat{x}, u) + l \cdot (\hat{y} - y) \quad (16a)$$

$$\hat{y} = c^T \cdot \hat{x}, \quad (16b)$$

with are A the system matrix, b , c the input and output vectors, l the observer gain vector containing negative values, u the input voltage v_D , and y the measurement θ . Due to the additional filter (14) for obtaining the amplitude Θ , the mirror state $\hat{\theta}$, $\hat{\dot{\theta}}$ is extended by the h -function to

$$\hat{x}^T = [\hat{\theta}, \hat{\dot{\theta}}, h, \dot{h}]^T. \quad (17)$$

With (11) and (14) the coefficients are

$$A(\hat{x}) = \begin{bmatrix} 0 & 1 & 0 & 0 \\ -\tilde{k}_n(\hat{x}_1) & -\tilde{c}_h(\hat{x}_3) & 0 & 0 \\ 0 & 0 & 0 & 1 \\ 0 & \omega_h^2 \hat{x}_2 & -\omega_h^2 & -2\omega_h \end{bmatrix}, \quad (18a)$$

$$b(\hat{x}, u) = \begin{bmatrix} 0 \\ \tilde{C}'(\hat{x}_1) u^2 \\ 0 \\ 0 \end{bmatrix}, \quad c = \begin{bmatrix} 1 \\ 0 \\ 0 \\ 0 \end{bmatrix}, \quad l^T = \begin{bmatrix} l_1 \\ l_2 \\ 0 \\ 0 \end{bmatrix}. \quad (18b)$$

The observer error dynamics [47] is $\dot{\hat{e}} = \hat{x} - \hat{\hat{x}}$ where the linear part has the characteristic polynomial

$$\det(sI - (A - l c^T)) = \lambda^2 + 2\lambda s + s^2. \quad (19)$$

For an asymptotic stable observer the linear gain coefficients considering neglectable small damping $c_n \approx 0$ are chosen to $l_1 = 2\lambda$, $l_2 = \lambda^2$, where the tuning parameter λ is above the mirror eigenfrequency ω_0 .

IV. EXPERIMENTAL VERIFICATION

The proposed charge sensing methods are verified using a 1D resonant MEMS mirror. The used MEMS mirror is a revised design of one in [11], [12], [48], which has an elliptical mirror shape of 2.7 mm major axis and the linear frequency is around 2 kHz. The mirror is designed for oscillating $\pm 15^\circ$

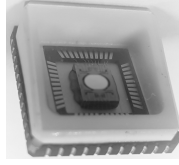


Fig. 6. Photograph of used uni-axial resonant MEMS mirror in a package

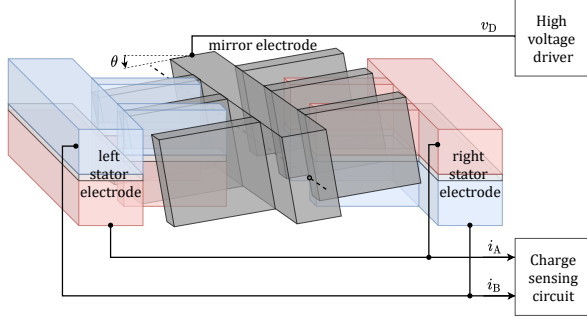


Fig. 7. Electrostatic comb drive configuration of used MEMS mirror featuring a single mirror electrode (gray) which can tilt by θ and two separated electrodes for each stator. This configuration allows the direction detection as shown with connections to the charge sensing circuit. The displacement current i_A is measured from the top left and bottom right electrodes (red). The displacement current i_B is measured from the bottom left and top right electrodes (blue).

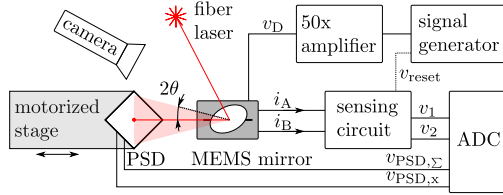


Fig. 8. Optical test bench setup for experimental verification

mechanical angle to span 60° field of view in lidar application. The detailed design concepts such as leaf spring, torsion bars, comb drive shapes are given in [48]. Further analysis of the mirror and driving concept of the MEMS mirror can be found in [49]. The direction detection is realized by a two layer design of the stator electrodes and a mirror drive electrode as shown in Fig. 7.

A. Experimental setup and implementation

The MEMS mirror deflection is measured optically in an experimental test bench shown in Fig. 8, as described in [14]. A fiber laser points on the MEMS mirror and reflects the beam on a 2D PSD (S5991-01, 2D PSD, Hamamatsu, Hamamatsu City, Japan), which is mounted on a motorized stage for optical alignment. The MEMS is mounted on a PCB with the sensing circuit. A camera is used for alignment of the laser spot on the mirror. All data is recorded with an ADC (U2531A, Agilent Technologies Inc.) at 2 MSa/s. All three charge sensing methods are realized with individual circuits (PCBs) as follows:

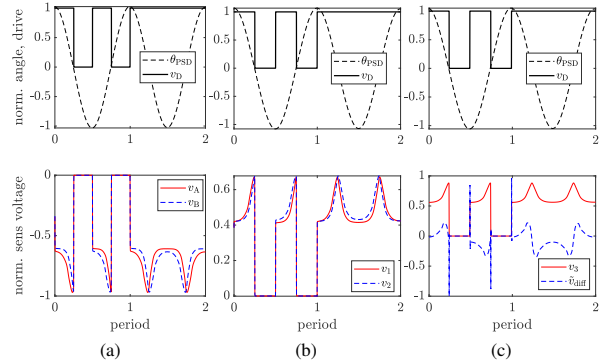


Fig. 9. Capacitance calibration measurements on the verge to actuated decay with constant voltage starting at period 1: (a) charge integrator, (b) series capacitance, (c) capacitance network

a) Current integrator: For the current integrator the integrated circuit (ACF2101, Burr-Brown) with internal reset switches and internal trimmed capacitors $C_{int} = 100$ pF are used. Therefore, the capacitors C_{int} are not treated differently for both channels.

b) Series capacitance: The series capacitance (Fig. 6) is provided with off-the-shelf SMD capacitances of nominal $C_1 = C_2 = 100$ pF. To minimize parasitic capacitances on the line to the ADC and the invasiveness of the measurement, two voltage follower (ADA4000, Analog Devices) are implemented for the outputs (Fig. 3b). Integrator reset is performed by switches (ADG1211, Analog Devices). For all measurements a time delay of twice the sampling time is considered.

c) Capacitance network: The capacitance network is implemented with off-the-shelf SMD capacitances of nominal $C_{1n} = C_{2n} = 1$ nF and $C_{3n} = 100$ pF. The difference voltage v_{diff} is measured with an instrumentation amplifier (LT1102, Analog Devices) between nodes 1 and 2 in Fig. 3c and a gain of 20. The sum signal v_3 is provided from node 3 in Fig. 3c after a voltage follower. The switches are applied for reset as well.

B. Charge sensing calibration

The charge sensing voltage-deflection relations are calibrated once in the test bench setup by an actuated decay measurement, i.e. after sweeping the mirror to maximum amplitude the drive voltage is switched to a constant high voltage [43]. During the subsequent mirror decay the charge sensing voltages (resp. comb drive charges) are measured continuously for at least 100 periods, cf. actuated decay after period 1 in Fig. 9. This capacitance calibration strategy is performed for each charge sensing concept described in Sec. II. Fig. 10b shows the actuated decay measurement for the charge integrator setup.

1) Leakage: The actuated decay measurements feature a voltage drop, i.e. the voltages at zero crossing angle vary over the measured 400 periods. This effect can be explained by parasitic resistances from the switch parallel to the measurement capacitances (e.g. C_{int} as well as C_1, C_2 or C_{1n}, C_{2n} ,

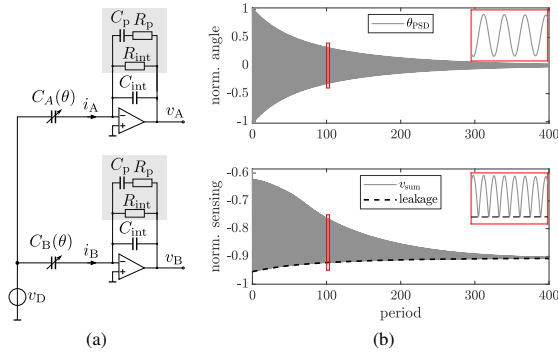


Fig. 10. Capacitance calibration using current integrator: (a) Equivalent circuit for model (20) with parasitic leakage circuit with $R_p = 5.666 \text{ G}\Omega$, $C_p = 4.875 \text{ pF}$, $R_{int} = 1000 \text{ G}\Omega$ in gray box; (b) actuated decay measurement with angle (upper) and sum voltage v_{sum} and leakage (lower), insets show the signals after 100 periods

C_{3n}) where a small current leaks. For the circuit with current integrator with internal switch a precise leakage model was found as transfer function $G_{leak}(s) = \frac{v_{sum,corr}}{v_{sum}}$ to be

$$G_{leak}(s) = \frac{\tau_{int}\tau_p s^2 + \tau_{int}s}{\tau_{int}\tau_p s^2 + (R_{int}C_p + \tau_{int} + \tau_p)s + 1}, \quad (20)$$

where $\tau_{int} = C_{int}R_{int}$ and $\tau_p = C_pR_p$ as depicted in Fig. 10a. The parameters in (20) are identified by minimizing the voltage drop of the actuated decay data to zero. Afterwards the leakage correction is applied with the dynamic time response of the system (20) using 'lsim' function from Matlab on the measurement data v_{sum} shown in Fig. 10b (lower).

$$C(\theta) = C_{int} \frac{v_{sum,corr}}{v_D} \quad (21)$$

The calibration capacitance function (21) results in an overlay of more than 400 periods with a residual fit root-mean-square-error (RMSE) of 0.02%, see Fig. 11a. The leakage correction is applied in the same way on the charge sensing data.

2) *Parasitic capacitances:* Additional parasitic capacitances C_{par} and C_{off} are considered for the series and network circuit, which might be originated from the switches, capacitance tolerances and wiring on the PCB.

For the series capacitance circuit parasitic capacitances are estimated to be $C_{par} = 34 \text{ pF}$ and $C_{off} = 1.05 \text{ pF}$, which matches well with the current integrator circuit results. Consequently, the capacitances are calibrated with

$$C_A(\theta) = \frac{(C_1 + C_{par})v_A(\theta)}{v_D - v_A(\theta)} + C_{off}, \quad (22)$$

$$C_B(\theta) = \frac{(C_2 + C_{par})v_B(\theta)}{v_D - v_B(\theta)} + C_{off}. \quad (23)$$

Similarly, the capacitance network circuit parameter are estimated to be $C_1 = 990 \text{ nF}$ and $C_2 = 990 \text{ nF}$ and $C_{off} = 1.2 \text{ pF}$ with

$$C(\theta) = 2 \cdot \left[\frac{C_3 v_{sum}(\theta)}{v_D - v_{sum}(\theta)} + C_{off} \right] \approx C_{net}(\theta). \quad (24)$$

These parasitics could be reduced by trimmed capacitors and an integrated circuit design for improved sensing accuracy.

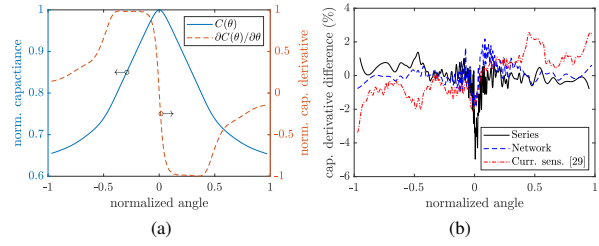


Fig. 11. Calibration result: (a) capacitance and derivative measured with current integrator circuit, (b) difference of capacitance derivative towards series and network circuit as well as current sensing for the same device

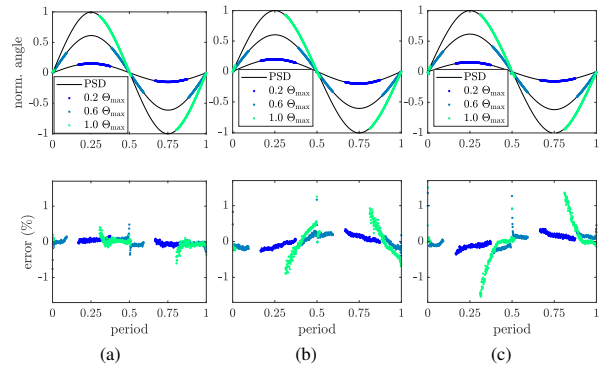


Fig. 12. Charge sensing measurements at three operation points ($0.2 \Theta_{max}$, $0.6 \Theta_{max}$ and full amplitude) with RMSE of 80 periods with respect to Θ_{max} : (a) current integrator, (b) series capacitances, (c) capacitance network

The calibrated sum capacitance and its derivative are shown in Fig. 11a. The good agreement of the calibrated capacitance derivative is validated comparing the current integrator result with series and network circuit as well as current sensing for the same device, where the residual error stay mainly below $\pm 2\%$, see Fig. 11b.

C. Charge sensing measurements

By applying the calibration capacitance $C(\theta)$ from the previous section to the charge sensing measurements the instantaneous angle is calculated with (6) for CI and Series circuit and (10) for Network circuit respectively. Fig. 12 shows these results and errors in comparison to the PSD measurement at several operation points (see + marks in Fig. 13) of the MEMS mirror. For lower response at $0.2 \Theta_{max}$ the high voltage is on, when the mirror is at high angle, while for upper response at $0.6 \Theta_{max}$ amplitude and full amplitude the high voltage is on, when the mirror angle crosses zero. Due to loading transients limiting the charging current at voltage on switch the first $20 \mu\text{s}$ are blanked out and not evaluated further. The RMSEs given in Tab. I are below 0.5% with respect to Θ_{max} for all three concepts and for the current integrator even below 0.06%, while for the other two methods the higher error might be caused by inaccuracies from the off-the-shelf capacitances or voltage follower circuit. For full

TABLE I
PEAK-TO-PEAK (PTP) AND RMS ERRORS IN PERCENT TOWARDS FULL AMPLITUDE $2\Theta_{\max}$ FOR CHARGE SENSING MEASUREMENTS OF FIG. 12

Θ_{\max}	CI		Series		Network	
	ptp/%	RMS/%	ptp/%	RMS/%	ptp/%	RMS/%
0.2	0.28	0.04	0.39	0.08	0.45	0.09
0.6	1.23	0.05	2.09	0.15	3.46	0.39
1.0	1.15	0.06	2.29	0.22	4.32	0.42

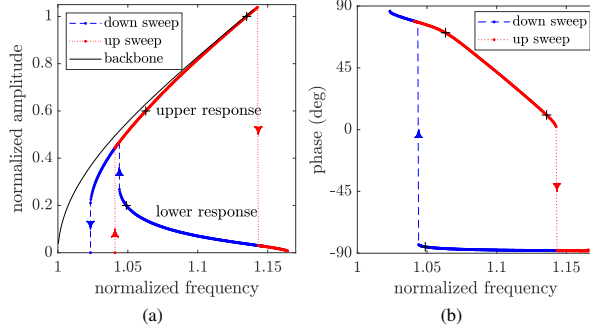


Fig. 13. Nonlinear behavior with bifurcation jumps for up/down frequency sweeps : (a) amplitude over frequency with measured backbone from free (non-actuated) decay, (b) phase over frequency. The phase is defined between the drive voltage switch off and the zero crossing of the mirror angle. Black plus signs refer to three operation points used for the charge sensing results.

angle estimation the full mirror observer model identification is described in the following.

D. Mechanical parameter identification

The mechanical parameter of stiffness and damping are identified from decay measurements without actuation, i.e. zero voltage, considering the nonlinear amplitude-frequency behavior. The mirror is designed for the mechanical scan amplitude of $\pm 15^\circ$ with a linear mirror frequency around 2 kHz. The strong non-linearity in stiffness, which is determined by the backbone curve as in Fig. 14a, arises from the leaf-spring design. The potential energy for every period inhering a specific frequency is matched to the amplitude at the backbone curve, as previously described in [43]. The spring torque is derived from the stiffness (12) by integration as

$$\tau(\theta) = \int k_n(\theta) d\theta. \quad (25)$$

First the stiffness k_0 and small eigenfrequency f_0 are found from decay data at small amplitudes. Afterwards the higher order stiffnesses k_2, k_4, k_6 are estimated by solving the least-square problem, which minimizes the difference between decay data $f(\Theta)$ of the backbone curve as shown in Fig. 14a towards a quarter sine period using

$$\min_{k_2, k_4, k_6} \left\| \frac{1}{f(\Theta_i)} - \frac{4}{\sqrt{2}} \int_0^{\Theta_i} \frac{d\theta'}{\sqrt{\tau(\Theta_i) - \tau(\theta')}} \right\|_2^2 \quad (26)$$

with the quarter sine period as

$$\theta(\Theta_i) = \Theta_i \sin(\Omega), \quad \Omega \in 0 \dots \frac{\pi}{2}. \quad (27)$$

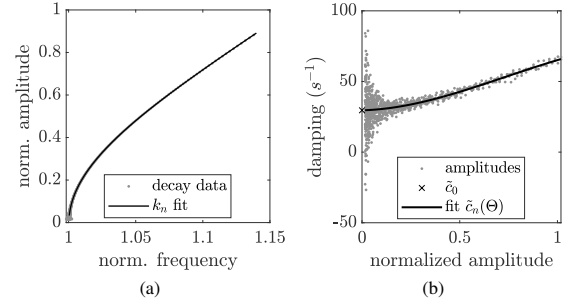


Fig. 14. Identified parameter: (a) backbone data set $f(\Theta)$ and fit for stiffness evaluation by potential energy matching with fit RMSE=0.45%, (b) damping over amplitude Θ according (28) and fit RMSE=6.3%

In 26 the term $\tau(\Theta_i)$ represents the total energy for the oscillation amplitude Θ_i and the term $\tau(\theta')$ is equivalent to the torque of a quarter period given by 27. The small damping influence is neglected. The approach results to a well matched fit for a 6th order polynomial fit as given in (12). Considering amplitudes above 0.2% Θ_{\max} , the fit error stays below 0.1 %, cf. Fig. 14a.

The damping coefficient is determined dependent from the current oscillation amplitude Θ by calculating the potential energy loss in the spring from the amplitude of each period to the next along the non-actuated decay [43] as

$$c_n(\Theta_i) = \frac{\int_{\Theta_{i+1}(t)}^{\Theta_i} \tau(\theta') d\theta'}{\int_{\Theta_{i+1}(t)}^{\Theta_i(t)} \dot{\theta}(t) dt}, \quad (28)$$

where the nominator represents the normalized dissipated energy per each cycle using the spring torque (25) and the denominator integrates the measured velocity $\theta(t)$ trajectory in the time span between the two amplitude maxima. This results in the nonlinear damping over the amplitude Θ and is fitted with a 6th order polynomial fit (13) as shown in Fig. 14b.

E. Observer simulation

The presented self-sensing methods are capable for full time state estimation using an observer (16) applying the model parameter described before. The sensing data at different operation points for all three methods is applied to the input of this observer by simulation and evaluated for consecutive 80 periods, cf. Fig. 5. The observer gain is set with $\lambda = 8\omega_0$. To ignore loading transients of the charge measurement data, each first 10% period time are discarded for the switched input additionally to the voltage off time. The observer error is well found below 1% for all three methods at different operation points as Fig. 15 shows. Furthermore, the observer RMSE given in Tab. II stays below 0.25 %, which proves high repeatability and low noise of the observer output.

V. DISCUSSION

In contrast to single point detection approaches, e.g. [32], [38], the presented charge self-sensing provides full state

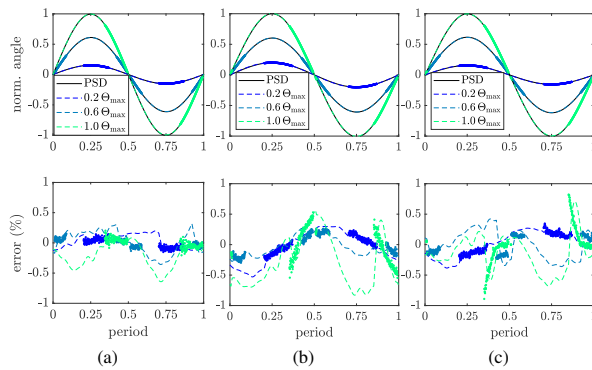


Fig. 15. Observer results (dashed line) and sensing data (dots) for three operation points ($0.2 \Theta_{\max}$, $0.6 \Theta_{\max}$ and full amplitude) with observer RMSE of 80 periods: (a) current integrator, (b) series capacitances, (c) capacitance network

TABLE II
PEAK-TO-PEAK (PTP) AND RMS ERRORS IN PERCENT TOWARDS FULL AMPLITUDE $2\Theta_{\max}$ FOR OBSERVER RESULTS OF FIG. 15

Θ_{\max}	CI		Series		Network	
	ptp/%	RMS/%	ptp/%	RMS/%	ptp/%	RMS/%
0.2	0.26	0.07	0.49	0.13	0.90	0.10
0.6	0.42	0.10	0.35	0.08	0.87	0.11
1.0	0.53	0.14	0.76	0.25	1.62	0.17

feedback, which is suitable for continuous precision feedback control, by applying the sensing data to an observer with switched input during the drive voltage on time. Additionally, the current integration performs intrinsic filtering of high frequency distortion, e.g. parasitic mechanical modes are attenuated and do not harm the accuracy of the measurement. The presented sensing methods collect the charge on the comb capacitance, which is implemented in three variants: a) a current integrator as integrated circuit, b) series capacitances and c) a capacitance network. To avoid long term integration offsets the periodical reset of the capacitances is indispensable, but the switches can also introduce parasitic current leakage. The CI circuit suffers by higher current leakage from the internal switch, but a precise calibration of the leakage results into the overall highest accuracy with less than $\pm 0.33\%$ peak-to-peak error and 0.14% RMSE. The second method collects the charge passively on a series capacitance, but imperfections from the off-the-shelf components lead to a less accurate calibration. However, this drawback might be solved by accurately trimmed or on-the-chip static comb capacitances, that provide a precise integration capacitance reference for C_{int} or C_1 , C_2 or C_{1n} , C_{2n} , C_{3n} respectively. The third method is attractive to reduce the high precision sensing channels to one (v_3), while the difference signal \tilde{v}_{diff} can be digital for the direction detection only. The presented charge sensing principles work independently from the phase relation between driving and mirror oscillation. Therefore, also linear stiffening mirrors without bifurcation can be sensed, in comparison to the phase detection presented in [43], where the angle zero crossing is required to be during high voltage time. Since the

charge-based self-sensing integrates even small displacement currents, the presented concept might be applicable for MEMS mirrors with lower eigenfrequencies in the range of hundreds of Hertz.

Charge-based capacitive self-sensing enables continuous angle estimation for electrostatic MEMS mirrors even with small frequencies or currents and independently of the phase relation or bifurcation state. The three variants of sensing circuits with active and passive current integration proposed in this work have been experimentally demonstrated to provide accurate angle estimation and continuous state estimation based on a switched observer.

VI. CONCLUSION

This paper demonstrates precise angle estimation of a resonant electrostatic MEMS mirror via capacitive charge self-sensing methods without additional modulation. The angle of the MEMS mirror can be measured by the stored charge in the comb drive capacitance, i.e. direct charge self-sensing. A minor vertical offset or asymmetry of the movable mirror towards the stator electrodes allows the detection of the direction from the left and right charge difference. Current integration by an operational amplifier can lead to current leakage and charge slope limitations. As solution, the presented series capacitance or capacitance network circuits are passively collecting the charge and thus do have less influence on the actuator by the measurement itself. Reset switches are applied to avoid long term integration offsets, but they can also introduce additional current leakage. A suitable leakage model was found achieving highly accurate calibration of the capacitance function. The capacitance calibration also shows good agreement with current sensing with high bandwidth. High precision angle measurements with peak-to-peak error $\pm 0.33\%$ and a RMSE 0.14% over 80 periods at different amplitudes are demonstrated.

State estimation is essential for precise control and synchronization of several axis or mirrors. Due to the fact, that the charge sensing measures only during high voltage on time of the parametrically driven resonant MEMS mirror, a solution for full state estimation using an observer with switched input is derived and evaluated. Continuous charge sensing with shorter or no voltage off time is part of current research. The nonlinearity of stiffness and damping parameters are identified accurately from decay measurements. The simulated resulting observer performance achieves full state estimation for all three charge sensing data sets with a peak-to-peak angle error below $\pm 1\%$ and a RMSE less than 0.5% at different amplitudes. The presented charge sensing performs similar at the upper as well as at the lower response of the bifurcating nonlinear amplitude curve. Therefore, it represents an efficient method for amplitude and phase estimation, which can be applied to stabilize and synchronize several axis or mirrors performing Lissajous or raster scan figures.

REFERENCES

- [1] S. T. S. Holmström, U. Baran, and H. Urey, "MEMS Laser Scanners: A Review," *Journal of Microelectromechanical Systems*, vol. 23, no. 2, pp. 259–275, Apr. 2014. [Online]. Available: <https://doi.org/10.1109/JMEMS.2013.2295470>

- [2] A. Wolter, S.-T. Hsu, H. Schenk, and H. K. Lakner, "Applications and requirements for MEMS scanner mirrors," in *MOEMS and Miniaturized Systems V*, vol. 5719. International Society for Optics and Photonics, Jan. 2005, pp. 64–76. [Online]. Available: <http://dx.doi.org/10.1117/12.600076>
- [3] H. W. Yoo, N. Druml, D. Brunner, C. Schwarzl, T. Thurner, M. Hennecke, and G. Schitter, "MEMS-based lidar for autonomous driving," *e & i Elektrotechnik und Informationstechnik*, vol. 135, no. 6, pp. 408–415, Oct. 2018. [Online]. Available: <https://doi.org/10.1007/s00502-018-0635-2>
- [4] T. Sandner, T. Grasshoff, M. Schwarzenberg, R. Schroedter, and H. Schenk, "Quasistatic microscanner with linearized scanning for an adaptive three-dimensional laser camera," *Journal of Micro/Nanolithography, MEMS, and MOEMS*, vol. 13, no. 1, p. 011114, 2014. [Online]. Available: <https://doi.org/10.1117/1.JMM.13.1.011114>
- [5] P. K. Shrestha, M. J. Pryn, J. Jia, J.-S. Chen, H. N. Fructuoso, A. Boev, Q. Zhang, and D. Chu, "Accommodation-Free Head Mounted Display with Comfortable 3D Perception and an Enlarged Eye-box," *Research*, vol. 2019, pp. 1–9, Aug. 2019. [Online]. Available: <https://doi.org/10.34133/2019/9273723>
- [6] V. Milanovic, A. Kasturi, and V. Hachtel, "High brightness MEMS mirror based head-up display (HUD) modules with wireless data streaming capability," in *SPIE OPTO*, W. Piyawattanametha and Y.-H. Park, Eds., San Francisco, California, United States, Feb. 2015, p. 93750A. [Online]. Available: <https://doi.org/10.1117/12.2082848>
- [7] A. C. L. Hung, H. Y. H. Lai, T.-W. Lin, S.-G. Fu, and M. S. C. Lu, "An electrostatically driven 2D micro-scanning mirror with capacitive sensing for projection display," *Sensors and Actuators A: Physical*, vol. 222, pp. 122–129, Feb. 2015. [Online]. Available: <https://doi.org/10.1016/j.sna.2014.10.008>
- [8] A. Merten, R. Schroedter, A. Dreyhaupt, T. Graßhoff, M. Schwarzenberg, S. Hugger, C. Schilling, J. Grahmann, and R. Ostendorf, "Quasi-statischer MOEMS-Gitterscanner zum spektralen Durchstimmen eines MIR-Quantenkaskadenlasers," *tm - Technisches Messen*, vol. 86, no. 3, Feb. 2019. [Online]. Available: <https://doi.org/10.1515/teme-2019-0006>
- [9] K. Hwang, Y.-H. Seo, J. Ahn, P. Kim, and K.-H. Jeong, "Frequency selection rule for high definition and high frame rate Lissajous scanning," *Scientific Reports*, vol. 7, no. 1, pp. 1–8, Oct. 2017. [Online]. Available: <https://doi.org/10.1038/s41598-017-13634-3>
- [10] T. Sandner, T. Grasshoff, M. Wildenhain, and H. Schenk, "Synchronized microscanner array for large aperture receiver optics of LIDAR systems," in *Proc. SPIE*, W. P. Harald Schenk, Ed., vol. 7594, 2010, pp. 75 940C–75 940C–12. [Online]. Available: <https://doi.org/10.1117/12.844923>
- [11] D. Brunner, H. W. Yoo, R. Schroedter, and G. Schitter, "Adaptive Lissajous Scanning Pattern Design by Phase Modulation," *submitted to Optics Express, OSA*, p. 9, 2021.
- [12] H. W. Yoo, R. Riegler, D. Brunner, S. G. Albert, T. Thurner, and G. Schitter, "Experimental Evaluation of Vibration Influence on a Resonant MEMS Scanning System for Automotive Lidars," *IEEE Transactions on Industrial Electronics*, pp. 1–1, 2021. [Online]. Available: <https://doi.org/10.1109/TIE.2021.3065608>
- [13] J. Grahmann, R. Schroedter, O. Kiethe, and U. Todt, "Vibration analysis of micro mirrors for LIDAR using on-chip piezo-resistive sensor," in *MOEMS and Miniaturized Systems XIX*, vol. 11293. International Society for Optics and Photonics, Feb. 2020, p. 1129308. [Online]. Available: <https://doi.org/10.1117/12.2551600>
- [14] H. W. Yoo, D. Brunner, T. Thurner, and G. Schitter, "MEMS Test Bench and Its Uncertainty Analysis for Evaluation of MEMS Mirrors," in *Proceeding of 8th IFAC Symposium on Mechatronic*, Vienna, Austria, 2019, p. 6. [Online]. Available: <https://doi.org/10.1016/j.ifacol.2019.11.648>
- [15] B. Portelli, I. Grech, J. Micallef, R. Farrugia, O. Casha, and E. Gatt, "Resonant micro-mirror oscillation amplitude measurement and all digital actuation," in *Symposium on Design, Test, Integration Packaging of MEMS and MOEMS (DTIP)*, Jun. 2020, pp. 1–4. [Online]. Available: <https://doi.org/10.1109/DTIP5112.2020.9139131>
- [16] V. Annovazzi-Lodi, M. Benedetti, S. Merlo, and M. Norgia, "Spot Optical Measurements on Micromachined Mirrors for Photonic Switching," *IEEE Journal of Selected Topics in Quantum Electronics*, vol. 10, no. 3, pp. 536–544, May 2004. [Online]. Available: <https://doi.org/10.1109/JSTQE.2004.830625>
- [17] M. Baumgart, M. Lenzhofer, M. P. Kremer, and A. Tortschanoff, "Integrated packaging of 2D MOEMS mirrors with optical position feedback," in *SPIE OPTO*, W. Piyawattanametha and Y.-H. Park, Eds., San Francisco, California, United States, Feb. 2015, p. 93750R. [Online]. Available: <https://doi.org/10.1117/12.2079219>
- [18] J. Grahmann, A. Dreyhaupt, C. Drabe, R. Schroedter, J. Kamenz, and T. Sandner, "MEMS-mirror based trajectory resolution and precision enabled by two different piezoresistive sensor technologies," in *SPIE OPTO*, W. Piyawattanametha and Y.-H. Park, Eds., San Francisco, California, United States, Mar. 2016, p. 976006. [Online]. Available: <https://doi.org/10.1117/12.2212965>
- [19] S. Gu-Stoppel, T. Giese, H.-J. Quenzer, U. Hofmann, and W. Benecke, "PZT-Actuated and -Sensed Resonant Micromirrors with Large Scan Angles Applying Mechanical Leverage Amplification for Biaxial Scanning," *Micromachines*, vol. 8, no. 215, 2017. [Online]. Available: <https://doi.org/10.3390/mi8070215>
- [20] S. Tadigadapa and K. Mateti, "Piezoelectric MEMS sensors: State-of-the-art and perspectives," *Measurement Science and Technology*, vol. 20, no. 9, p. 092001, Jul. 2009. [Online]. Available: <https://doi.org/10.1088/0957-0233/20/9/092001>
- [21] D. Xia, C. Yu, and L. Kong, "The Development of Micromachined Gyroscope Structure and Circuitry Technology," *Sensors*, vol. 14, no. 1, pp. 1394–1473, Jan. 2014. [Online]. Available: <https://doi.org/10.3390/s140101394>
- [22] A. Utz, C. Walk, N. Haas, T. Fedtschenko, A. Stanitzki, M. Mokhtari, M. Görtz, M. Kraft, and R. Kokozinski, "An ultra-low noise capacitance to voltage converter for sensor applications in 0.35 μ m CMOS," *Journal of Sensors and Sensor Systems*, vol. 6, no. 2, pp. 285–301, Aug. 2017. [Online]. Available: <https://doi.org/10.5194/jsss-6-285-2017>
- [23] M. Lobur and A. Holovaty, "Overview and analysis of readout circuits for capacitive sensing in MEMS gyroscopes (MEMS angular velocity sensors)," in *2009 5th International Conference on Perspective Technologies and Methods in MEMS Design*, Apr. 2009, pp. 161–163. [Online]. Available: <https://ieeexplore.ieee.org/document/5069739>
- [24] F. Aezinia, "Design of Interface Circuits for Capacitive Sensing Applications," Thesis, Applied Sciences: School of Mechatronic Systems Engineering, Aug. 2014. [Online]. Available: <https://summit.sfu.ca/item/14460>
- [25] M.-H. Bao, *Handbook of Sensors and Actuators*. Elsevier, 2000, vol. 8, ch. Electrostatic Driving and Capacitive Sensing, pp. 139–198. [Online]. Available: [https://doi.org/10.1016/S1386-2766\(00\)80018-3](https://doi.org/10.1016/S1386-2766(00)80018-3)
- [26] Sheng-Yu Peng, M. Qureshi, P. Hasler, A. Basu, and F. Degertekin, "A Charge-Based Low-Power High-SNR Capacitive Sensing Interface Circuit," *IEEE Transactions on Circuits and Systems I: Regular Papers*, vol. 55, no. 7, pp. 1863–1872, Aug. 2008. [Online]. Available: <https://doi.org/10.1109/TCSI.2008.918006>
- [27] M. Saukoski, "System and Circuit Design for a Capacitive MEMS Gyroscope," Ph.D. dissertation, Helsinki University of Technology, Faculty of Electronics, Communications and Automation, Helsinki, 2008. [Online]. Available: <http://lib.tkk.fi/Diss/2008/isbn9789512292974/>
- [28] Y. Chen, H. Li, Z. Qiu, T. Wang, and K. R. Oldham, "Improved Extended Kalman Filter Estimation using Threshold Signal Detection with a MEMS Electrostatic Micro-Scanner," *IEEE Transactions on Industrial Electronics*, pp. 1–1, 2019. [Online]. Available: <https://doi.org/10.1109/TIE.2019.2901663>
- [29] U. Hofmann, J. Janes, and H.-J. Quenzer, "High-Q MEMS Resonators for Laser Beam Scanning Displays," *Micromachines*, vol. 3, no. 2, pp. 509–528, Jun. 2012. [Online]. Available: <https://doi.org/10.3390/mi3020509>
- [30] C. Xia, D. Qiao, X. Song, X. Song, W. Zheng, Y. He, and B. Wu, "A time division capacitive feedback method of electrostatic MEMS mirror driven by PWM signal," *Sensors and Actuators A: Physical*, vol. 322, p. 112631, May 2021. [Online]. Available: <https://doi.org/10.1016/j.sna.2021.112631>
- [31] D. Brunner, H. W. Yoo, and G. Schitter, "Linear Modeling and Control of Comb-Actuated Resonant MEMS Mirror with Nonlinear Dynamics," *IEEE Transactions on Industrial Electronics*, pp. 1–1, 2020. [Online]. Available: <https://doi.org/10.1109/TIE.2020.2982124>
- [32] —, "Precise phase control of resonant MOEMS mirrors by Comb-Drive current feedback," *Mechatronics*, vol. 71, p. 102420, Nov. 2020. [Online]. Available: <https://doi.org/10.1016/j.mechatronics.2020.102420>
- [33] R. Schroedter, K. Janschek, and T. Sandner, "Jerk and Current Limited Flatness-based Open Loop Control of Foveation Scanning Electrostatic Micromirrors," in *IFAC Proceedings Volumes*, vol. 47, Cape Town, South Africa, 2014, pp. 2685–2690. [Online]. Available: <https://doi.org/10.3182/20140824-6-ZA-1003.02566>
- [34] B. Cagdaser, A. Jog, M. Last, B. S. Leibowitz, L. Zhou, E. Shelton, and B. E. Boser, "Capacitive Sense Feedback Control for MEMS Beam Steering Mirrors," in *Proc. of Solid-State Sensor, Actuator and Microsystems Workshop, Hilton Head Island, South Carolina, USA*, 2004, pp. 6–10. [Online]. Available: <https://doi.org/10.1117/12.2079219>

- [//www.academia.edu/download/41600630/CAPACITIVE_SENSE_FEEDBACK_CONTROL_FOR_ME20160126-20127-1hznc74.pdf](http://www.academia.edu/download/41600630/CAPACITIVE_SENSE_FEEDBACK_CONTROL_FOR_ME20160126-20127-1hznc74.pdf)
- [35] L. J. Chemmunda, C. C. Jianrong, R. P. Singh, and Y. Roterman, "ASIC front-end for sensing MEMS-mirror position," in *2014 International Symposium on Integrated Circuits (ISIC)*, 2014, pp. 396–399. [Online]. Available: <https://doi.org/10.1109/ISICIR.2014.7029484>
 - [36] D.-D. Pham, R. P. Singh, Dan-Lei Yan, Kei-Tee Tiew, O. D. Bernal, T. Langer, A. Hirshberg, and Minkyu Je, "Position sensing and electrostatic actuation circuits for 2-D scanning MEMS micromirror," in *2011 Defense Science Research Conference and Expo (DSR)*. Singapore, Singapore: IEEE, Aug. 2011, pp. 1–4. [Online]. Available: <https://doi.org/10.1109/DSR.2011.6026861>
 - [37] Y. Chen, M. Lee, M. B. Birla, H. Li, G. Li, X. Duan, T. D. Wang, and K. R. Oldham, "Motion Estimation for a Compact Electrostatic Microscanner via Shared Driving and Sensing Electrodes in Endomicroscopy," *IEEE/ASME Transactions on Mechatronics*, vol. 25, no. 2, pp. 661–672, Apr. 2020. [Online]. Available: <https://doi.org/10.1109/TMECH.2020.2974969>
 - [38] K.-U. Roscher, U. Fakesch, H. Schenk, H. K. Lakner, and D. Schleich, "Driver ASIC for synchronized excitation of resonant micromirrors," in *MOEMS Display and Imaging Systems*, vol. 4985. International Society for Optics and Photonics, Jan. 2003, pp. 121–131. [Online]. Available: <https://doi.org/10.1117/12.477810>
 - [39] R. Schroedter, H. W. Yoo, D. Brunner, and G. Schitter, "Capacitive Charge-based Self-Sensing for Resonant Electrostatic MEMS mirrors," in *Proceedings of 21st IFAC World Congress*, Berlin, 2020.
 - [40] K. Janschek, *Mechatronic Systems Design - Methods, Models, Concepts*. Springer, 2012. [Online]. Available: <https://doi.org/10.1007/978-3-642-17531-2>
 - [41] H. v. Lierop, A. Hulsker, and J. Verheggen, "Monitoring of mems mirror properties," US Patent US20200132981A1, Apr., 2020. [Online]. Available: <https://patents.google.com/patent/US20200132981A1/en>
 - [42] I. Maksymova, P. Greiner, L. C. Niedermueller, and N. Druml, "Detection and Compensation of Periodic Jitters of Oscillating MEMS Mirrors used in Automotive Driving Assistance Systems," in *2019 IEEE Sensors Applications Symposium (SAS)*. Sophia Antipolis, France: IEEE, Mar. 2019, pp. 1–5. [Online]. Available: <https://doi.org/10.1109/SAS.2019.8706008>
 - [43] D. Brunner, H. W. Yoo, T. Thurner, and G. Schitter, "Data based modelling and identification of nonlinear SDOF MOEMS mirror," in *MOEMS and Miniaturized Systems XVIII*, vol. 10931. International Society for Optics and Photonics, Mar. 2019, p. 1093117. [Online]. Available: <https://doi.org/10.1117/12.2508429>
 - [44] D. Van Lierop and K. S. Khah, "Mirror device having leaf spring with openings," US Patent US20190129163A1, May, 2019. [Online]. Available: <https://patents.google.com/patent/US20190129163A1/en>
 - [45] T. Klose, T. Sandner, H. Schenk, and H. Lakner, "Extended damping model for out-of-plane comb driven micromirrors," in *Proc. SPIE*, vol. 6114, 2006, pp. 61140J–61140J–12. [Online]. Available: <https://doi.org/10.1117/12.645981>
 - [46] R. Farrugia, B. Portelli, I. Grech, D. Camilleri, O. Casha, J. Micallef, and E. Gatt, "Air damping of high performance resonating micromirrors with angular vertical comb-drive actuators," *Microsystem Technologies*, Apr. 2019. [Online]. Available: <https://doi.org/10.1007/s00542-019-04416-0>
 - [47] T. Meurer, K. Graichen, and E.-D. Gilles, Eds., *Control and Observer Design for Nonlinear Finite and Infinite Dimensional Systems*, ser. Lecture Notes in Control and Information Sciences. Berlin ; New York: Springer, 2005, no. 322. [Online]. Available: <https://doi.org/10.1007/11529798>
 - [48] H. W. Yoo, S. Albert, and G. Schitter, "Accurate Analytic Model of a Parametrically Driven Resonant MEMS Mirror With a Fourier Series-Based Torque Approximation," *Journal of Microelectromechanical Systems*, pp. 1–12, 2020. [Online]. Available: <https://doi.org/10.1109/JMEMS.2020.3024752>
 - [49] I. Maksymova, P. Greiner, J. Wiesmeier, F. M. Darrer, and N. Druml, "A MEMS mirror driver ASIC for beam-steering in scanning MEMS-based LiDAR," in *Laser Beam Shaping XIX*, A. Dudley and A. V. Laskin, Eds. SPIE, sep 2019. [Online]. Available: <https://doi.org/10.1117/12.2528312>



Richard Schroedter is a postdoctoral researcher in Advanced Mechatronic Systems at the Automation and Control Institute (ACIN) of TU Wien. He received his MSc in Mechatronics (2013) and his PhD degree (2018) from TU Dresden, Germany. For his doctoral thesis he worked at Fraunhofer Institute for Photonic Microsystems (IPMS) in Dresden, investigating the control of quasi-static MEMS mirrors. His primary research interests are high-precision mechatronic systems and microsystems for imaging and industrial automation.



Han Woong Yoo is postdoctoral researcher in Advanced Mechatronic Systems at the Automation and Control Institute (ACIN) of TU Wien. He received BSc from Yonsei University and MSc in Electrical Engineering from Seoul National University in 2007. Afterwards, he worked in Samsung Advanced Institute of Technology (SAIT) and Samsung Electronics co. LTD, semi-conductor business for low power digital RF and algorithms for reliability of multi-level non-volatile memories. He received PhD in 2015 at Delft University of Technology about optomechanics and adaptive optics for confocal microscopy. His main research interests are optical metrology, precision mechatronics systems, and biomedical imaging.



David Brunner is PhD student at the Automation and Control Institute (ACIN) of TU Wien. He received his MSc. degree in Energy Systems and Automation Technology from TU Wien, Austria, in 2017. His primary research interests include advanced identification and control concepts, high performance mechatronic systems and system integration.



Georg Schitter is Professor for Advanced Mechatronic Systems at the Automation and Control Institute (ACIN) of TU Wien. He received an MSc in Electrical Engineering from TU Graz, Austria (2000) and an MSc and PhD degree from ETH Zurich, Switzerland (2004). His primary research interests are on high-performance mechatronic systems, particularly for applications in the high-tech industry, scientific instrumentation, and mechatronic imaging systems, such as AFM, scanning laser and LIDAR systems, telescope systems, adaptive optics, and lithography systems for semiconductor industry. He received the journal best paper award of IEEE/ASME Transactions on Mechatronics (2017), of the IFAC Mechatronics (2008–2010), of the Asian Journal of Control (2004–2005), and the 2013 IFAC Mechatronics Young Researcher Award. He served as an Associate Editor for IFAC Mechatronics, Control Engineering Practice, and for the IEEE Transactions on Mechatronics.